Calculation of band alignments and quantum confinement effects in zero- and one-dimensional pseudomorphic structures

Min Yang and J. C. Sturm

Department of Electrical Engineering, Princeton University, Princeton, New Jersey 08540

Jean Prevost

Department of Civil Engineering and Operations Research, Princeton University, Princeton, New Jersey 08540

The strain field distributions and band lineups of zero-dimensional and one-dimensional strained pseudomorphic semiconductor particles inside a three-dimensional matrix of another semiconductor have been studied. The resulting strain in the particle and the matrix leads to band alignments considerably different from that in the conventional two-dimensional (2D) pseudomorphic growth case. The models are first applied to an ideal spherical and cylindrical $Si_{1-x}Ge_x$ particle in a large Si matrix. In contrast to the 2D case, the band alignments for both structures are predicted to be strongly type II, where the conduction-band edge and the valence-band edge of the Si matrix are both significantly lower than those in the $Si_{1-x}Ge_x$ inclusion, respectively. Band lineups and the lowest electron–heavy-hole transition energies of a pseudomorphic V-groove $Si_{1-x}Ge_x$ quantum wire inside a large Si matrix have been calculated numerically for different size structures. The photoluminescence energies of a large $Si_{1-x}Ge_x$ V-groove structure on Si will be lower than those of conventional 2D strained $Si_{1-x}Ge_x$ for similar Ge contents. [S0163-1829(97)04528-1]

I. INTRODUCTION

There has recently been an increasing interest in zero-dimensional (0D) quantum dots and one-dimensional (1D) quantum wires consisting of a pseudomorphically strained epitaxial semiconductor surrounded by a matrix of a second semiconductor. Such material systems include $Si_{1-x}Ge_x$ on Si (Refs. 1 and 2) and $In_xGa_{1-x}As$ on GaAs.[3–6] While the effect of uniform strain in biaxially strained pseudomorphic two-dimensional (2D) layers on planar substrates is well known,[7,8] the effect of strain on band alignments in pseudomorphic 0D and 1D particles generally has not been explored.

In this paper we first calculate the spatially varying strain fields and resulting band alignments for ideal spherical and cylindrical pseudomorphic inclusions in an infinite matrix and apply the results to $Si_{1-x}Ge_x$ in Si assuming that the materials are isotropic. The results are very different from those in a uniform biaxially strained 2D layer and the type of the band offset (type I vs type II) can be changed. The finite-element method is then used to investigate the strain distribution in and around a single V-groove $Si_{1-x}Ge_x$ quantum wire buried inside a large Si matrix. The electron and hole energy levels are obtained in order to compare with experimental photoluminescence values.

In the following section we will first discuss analytical strain distributions for ideal symmetry structures, i.e., pseudomorphic 0D spheres and 1D cylinders made up of isotropic materials. In Sec. III we will present the approach to calculate band alignments from the strain distributions following the *model-solid approach* of Van de Walle and Martin[7,8] and Pollak and Cardona.[9] The results for pseudomorphic $Si_{1-x}Ge_x$ inside a Si matrix using the analytic models are given in Sec. IV. The analytic results are also compared with results where the strain is calculated numerically using the finite-element approach taking anisotropies into account. Numerical results are derived in Sec. V for a V-groove $Si_{1-x}Ge_x$ quantum wire, considering the anisotropic elastic properties of $Si_{1-x}Ge_x$ material. A perturbation approach is used to get the quantum confinement energy in the small V grooves.

II. STRAIN DISTRIBUTION OF IDEAL STRUCTURES

In order to determine the band alignments of a system, the strain distribution in the space is required. For the purposes of an analytical calculation it is assumed at first that the elastic properties of Si and Ge are isotropic. The results will be compared with the anisotropic case later. We also consider only the ideal pseudomorphic interface.

A. Spheres

Conceptually, a pseudomorphic 0D dot can be formed by replacing atoms in a sphere of radius R in an infinite matrix of a semiconductor with atoms of a second semiconductor of different lattice constant. If the lattice constant of the relaxed inclusion a_i is larger (smaller) than that of the matrix a_m, both materials are under compressive (tensile) stress. This was modeled using continuum linear elastic theory assuming no defects or plastic deformation. The problem of an isotropic spherical inclusion inside an isotropic matrix was solved by Eshelby[10,11] to the first order of the lattice mismatch between the inclusion and the matrix $\epsilon_m = a_i/a_m - 1$. In the inclusion, only a uniform hydrostatic strain exists, with a value of

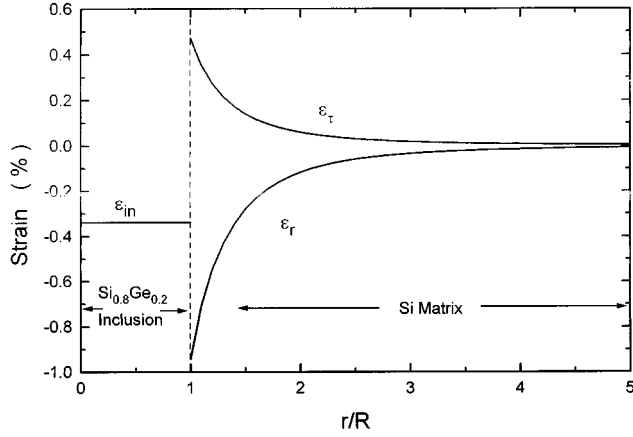$$\varepsilon_{in} = \epsilon_m \left(\frac{1}{\gamma} - 1 \right), \tag{1a}$$

FIG. 1. Strain distribution vs r/R ratio of the distance over the radius of the sphere for the structure of a $Si_{0.8}Ge_{0.2}$ sphere inside a Si matrix. ε_τ and ε_r are the tangential and radial strain components. The strain inside SiGe is uniform and hydrostatic.

where $\gamma = 1 + 2K_m(1 - 2\nu_m)/K_i(1 + \nu_m)$, K_i and K_m represent the bulk modulus of the inclusion and the matrix, and ν_m is the Poisson ratio of the matrix. In the matrix, only "normal" (no shear) strains exist, in both the radial and tangential directions, which are given by

$$\varepsilon_r = -2\frac{\epsilon_m}{\gamma}\left(\frac{R}{r}\right)^3, \tag{1b}$$

$$\varepsilon_\tau = \frac{\epsilon_m}{\gamma}\left(\frac{R}{r}\right)^3. \tag{1c}$$

The strain in the matrix has no hydrostatic component; its magnitude is independent of the absolute size of the sphere, but only related to r/R, the ratio of the distance from the center and the radius of the sphere. Note that the result pertains only to isolated spheres, not to an interaction array of spheres.

The strain components ε_r and ε_τ are plotted in Fig. 1 for a $Si_{0.8}Ge_{0.2}$ sphere inside an infinite Si matrix. The uniformly distributed hydrostatic strain inside the sphere is -3.4×10^{-3} and in the matrix around the sphere the radial and tangential strain components are -9.4×10^{-3} and 4.7×10^{-3}, respectively. In real materials, the size of the matrix is finite. In the case of a finite spherical matrix, the strain field also may be found analytically.[12] Figure 2 gives the value of the hydrostatic strain inside the $Si_{0.8}Ge_{0.2}$ inclusion as a function of the ratio between the radius of the matrix and the inclusion R_{Si}/R_{SiGe}. The strain inside SiGe decreases as the size of the matrix decreases. But at $R_{Si}/R_{SiGe} = 3$, the strain inside the sphere is already 97% of the value of the infinite model. Therefore, the magnitude of strain distribution can be estimated using an infinite matrix as long as the radius of the matrix R_{Si} is several times larger than the radius of the SiGe sphere R_{SiGe}.

B. Cylinders

To model a 1D structure, an infinitely long (in the z direction) cylindrical-shaped inclusion with radius R is in-
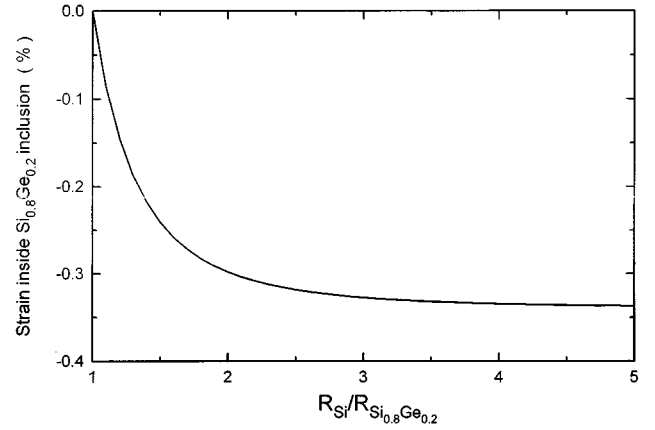

FIG. 2. Strain inside a $Si_{0.8}Ge_{0.2}$ sphere as a function of $R_{Si}/R_{Si_{0.8}Ge_{0.2}}$, the ratio of the radius of the Si matrix over the SiGe sphere. The infinite matrix approximation is good for R_{Si} several times larger than R_{SiGe}.

serted in an infinite matrix of smaller (larger) lattice constant. For a pseudomorphic structure, the axial strain in the matrix is

$$\varepsilon_{zz} = 0. \tag{2a}$$

The radial and tangential strain components in the matrix are[12]

$$\varepsilon_r = -\frac{\epsilon_m}{\gamma'}\left(\frac{R}{r}\right)^2, \tag{2b}$$

$$\varepsilon_\tau = \frac{\epsilon_m}{\gamma'}\left(\frac{R}{r}\right)^2 \tag{2c}$$

and in the cylinder

$$\varepsilon_{zz} \approx -\epsilon_m, \tag{2d}$$

$$\varepsilon_r = \varepsilon_\tau = \epsilon_m\left(\frac{1}{\gamma'} - 1\right), \tag{2e}$$

with

$$\gamma' = \frac{1}{1 + \nu_i} + \frac{K_m}{K_i}\frac{1 - 2\nu_m}{1 + \nu_m}.$$

For a $Si_{0.8}Ge_{0.2}$ cylinder inside a Si matrix, the strain components are plotted in Fig. 3. The strain ε_r and ε_τ inside the cylinder would be -1.01×10^{-3} with a lattice mismatch of -8.1×10^{-3} in the z direction. In the matrix ε_r and ε_τ are -7.1×10^{-3} and 7.1×10^{-3}, respectively, at the boundary.

III. CALCULATION OF BAND ALIGNMENTS FOR STRAIN DISTRIBUTION

To determine the effect of strain on band alignments, we first define the xyz axis for our analysis in the usual [100], [010], and [001] crystal directions. The procedure for obtaining the lineups follows the *model-solid approach* of Van de Walle and Martin.[7,8] In this theory the average energy of highest valence bands at the Γ point $E^0_{v,av}$ is set on an absolute scale for bulk relaxed material. The effect of spin-orbit

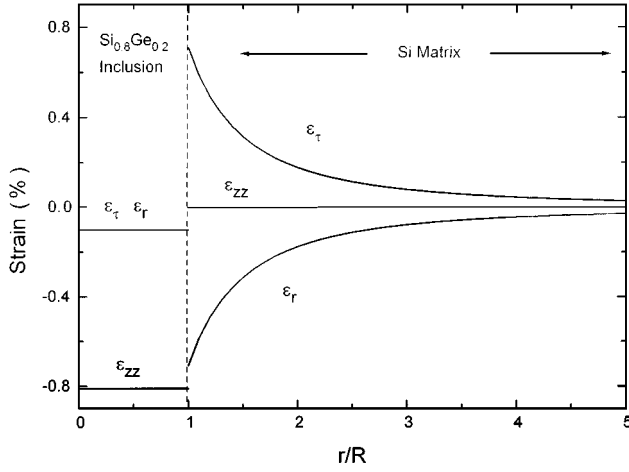FIG. 3. Strain distribution vs r/R ratio of the distance over the radius of the cylinder for the structure of a $Si_{0.8}Ge_{0.2}$ cylinder inside a Si matrix. ϵ_τ and ϵ_r are the tangential and radial strain components in the polar plan. ϵ_{zz} is the axial strain.

coupling (H_{so}, assumed to be independent of strain) and the effects of strain (H_ε) are then added to this starting point to get the position of an individual valence-band maximum:

$$E_v = E_{v,av}^0 + \langle J, m_J | H_{so} + H_\varepsilon | J, m_J \rangle. \tag{3}$$

The sixfold degeneracy of the valence-band maximum (assumed at the Γ point) in bulk material is split by the spin-orbit interaction into a fourfold multiplet ($J = 3/2$, $m_J = \pm 3/2, \pm 1/2$, and $H_{so} = +\Delta_0/3$) and a twofold multiplet ($J = 1/2$, $m_J = \pm 1/2$, and $H_{so} = -2\Delta_0/3$), where Δ_0 is the spin-orbit splitting. The orbital-strain Hamiltonian H_ε for a given band at the Γ point is[9]

$$H_\varepsilon = a_v(\varepsilon_{xx} + \varepsilon_{yy} + \varepsilon_{zz}) - 3b[(L_x^2 - \tfrac{1}{3}\mathbf{L}^2)\varepsilon_{xx} + \text{c.p.}]$$
$$- \sqrt{3}d[(L_xL_y + L_yL_x)\varepsilon_{xy} + \text{c.p.}], \tag{4}$$

where the parameter a_v represents the hydrostatic deformation potential for the valence band. The quantities b and d are uniaxial-deformation potentials, $\mathbf{L}$ is the angular momentum operator, and c.p. denotes cyclic permutation. Note that strain might shift the average valence-band position ($E_{v,av}^0$ is for unstrained material) and lift the degeneracy between $|3/2, \pm 3/2\rangle$ and $|3/2, \pm 1/2\rangle$ states.

For the conduction band, the absolute energy of the minimum of conduction-band valley j of type Δ, L, or Γ (repre-

sented by α), $E_{c,\alpha}^j$, is determined by adding the shift of the minimum due to strain $\Delta E_{c,\alpha}^j$ to the position of the conduction-band minimum in bulk material $E_{\alpha,av}^0$, where

$$E_{\alpha,av}^0 = E_{g,\alpha}^0 + \frac{\Delta_0}{3} + E_{v,av}^0 \tag{5}$$

and

$$E_{c,\alpha}^j = \Delta E_{c,\alpha}^j + E_{\alpha,av}^0. \tag{6}$$

$E_{g,\alpha}^0$ is the distance from the valence-band maximum to the minimum of the conduction band of type α in relaxed bulk material. $\Delta E_{c,\alpha}^j$ can be written as[8]

$$\Delta E_{c,\alpha}^j = [\Xi_d^\alpha \overleftrightarrow{1} + \Xi_u^\alpha \hat{\mathbf{a}}_j \hat{\mathbf{a}}_j] : \overleftrightarrow{\varepsilon}, \tag{7}$$

where $\overleftrightarrow{1}$ is the unit tensor, $\hat{\mathbf{a}}_j$ is the unit vector to the valley j, $\overleftrightarrow{\varepsilon}$ is the strain tensor, and Ξ_d^α and Ξ_u^α are the deformation potentials for conduction band α. The quantity $\Xi_d^\alpha + \tfrac{1}{3}\Xi_u^\alpha$, sometimes also denoted as a_c^α, is the hydrostatic deformation potential for the conduction band α. The degeneracies of conduction-band minima not at Γ (e.g., Δ and L) are usually split by nonhydrostatic strain; conduction-band minima at Γ are only subject to hydrostatic strain shifts [the second term on the right-hand side in Eq. (7) vanishes].

IV. IDEAL SYMMETRIC STRUCTURES OF $Si_{1-x}Ge_x/Si$

We now apply these formulas to the case of a single $Si_{1-x}Ge_x$ sphere and cylinder inside a Si matrix. The parameters used are listed in Table I. All were linearly interpolated for the alloys except $E_{v,av}^0$ and $E_{g,\alpha}^0$. In an alloy $A_{1-x}B_x$ with lattice constants a_A and a_B mismatched, $E_{v,av}^0$ should be given by[8]

$$E_{v,av}^0(x) = xE_{v,av,B}^0 + (1-x)E_{v,av,A}^0$$
$$+ 3x(1-x)[-a_v^B + a_v^A]\frac{a_B - a_A}{a_{AB}}, \tag{8}$$

where the alloy lattice constant $a_{AB} = a_A(1-x) + a_Bx$. The band gaps of the bulk relaxed alloys were fit with a quadratic as

$$E_{g,\alpha}^0(x) = (1-x)E_{g,\alpha,A}^0 + xE_{g,\alpha,B}^0 - c_\alpha x(1-x), \tag{9}$$

where α refers to the type of conduction-band minimum and c_α is a "bowing" parameter.

TABLE I. Lattice constant a (in angstroms), elastic constants c_{11}, c_{12}, and c_{44} (in 10^{12} dyn/cm^2), spin-orbit splitting Δ_0, average valence band $E_{v,av}^0$, band gaps $E_{g,\Delta}^0$, $E_{g,L}^0$, and $E_{g,\Gamma}^0$, and deformation potentials a_v, b, d, Ξ_u^Δ, Ξ_u^L, Ξ_d^Δ, Ξ_d^L, and Ξ_d^Γ (all in eV) used in this work (Refs. 7 and 8 except where noted).

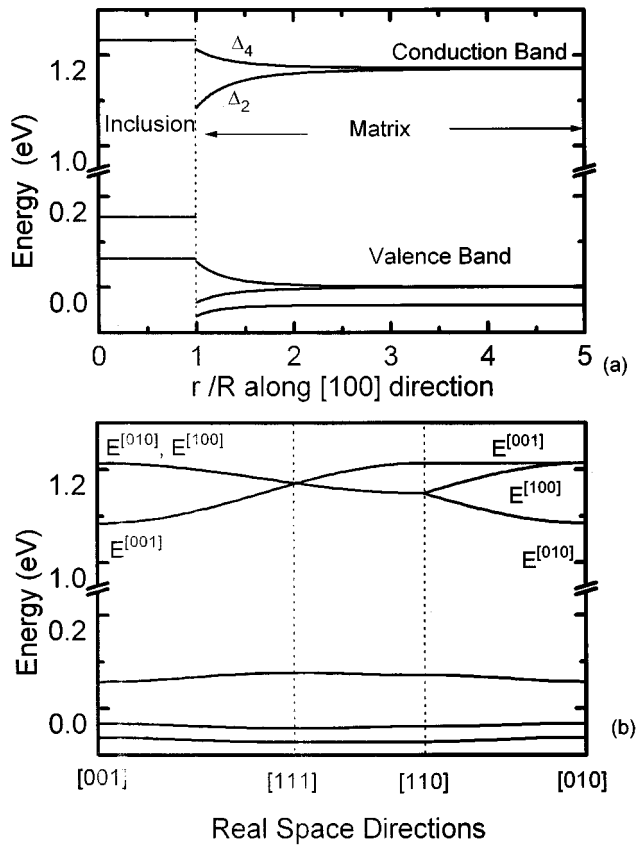| | a | c_{11} | c_{12} | c_{44} | $E_{g,\Gamma}^0$ | $E_{g,\Delta}^0$ | $E_{g,L}^0$ | Δ_0 | $E_{v,av}^0$ | c_Γ |
	a_v	b	d	Ξ_u^Δ	Ξ_u^L	Ξ_d^Δ	Ξ_d^L	Ξ_d^Γ	c_L	c_Δ
Si	5.43	1.675	0.650	0.801	3.37	1.17	2.06	0.04	-7.03	
	2.46	-2.35	-5.32	9.16	16.14	1.127	-6.04	1.98	0.0^a	0.206^a
Ge	5.65	1.315	0.494	0.684	0.89	0.96	0.74	0.3	-6.35	
	1.24	-2.55	-5.50	9.42	15.13	-0.59	-6.58	-8.24	0.0^a	0.206^a

[a]Reference 19.

FIG. 4. (a) Band positions vs r/R in the [100] direction for the 0D system: a $Si_{0.8}Ge_{0.2}$ sphere inside a Si matrix. All energies are referred to the top of the valence band in Si bulk material. Only the Δ conduction band is plotted here. (b) Energy bands vs real-space direction in the matrix at $r = R$.

A. $Si_{1-x}Ge_x$ quantum wires and quantum dots

For the case of a $Si_{0.8}Ge_{0.2}$ sphere in a Si matrix, Fig. 4(a) gives the band extrema positions as a function of r/R in the [100] real-space direction, which has the lowest conduction band. (Note that the [100], [010], and [001] directions are equivalent in this spherical inclusion case.) The energies are relative to the top of the valence-band edge in relaxed Si material. Only Δ conduction bands are plotted as L bands lie higher in energy for all Ge concentrations (unlike the relaxed alloy), assuming the L band gap in bulk Si of 2.06 eV. Inside the sphere, the band edges of SiGe are uniform due to the uniform strain distribution. As the stress in the sphere is hydrostatic, the conduction-band and the valence-band edges remain degenerate except for the spin-orbit splitting of the valence band, although both bands are dropped from their relaxed positions. In the Si matrix, the fourfold-degenerate conduction band Δ_4 is lifted up by 0.045 eV and the twofold-degenerate conduction band Δ_2 (valleys in the [100] and [$\bar{1}$00] k-space directions for the [100] real-space direction) drops by 0.09 eV to form the conduction-band minimum. As there is no hydrostatic strain in the matrix, the weighted average of these bands does not change. At the boundary, the conduction-band edge in the matrix is 0.15 eV lower than that inside the sphere and the valence-band edge in the sphere lies 0.10 eV higher than that outside the sphere. Although it is well known that for biaxially strained planar

$Si_{1-x}Ge_x$ on Si(100) substrates the conduction-band offset is negligibly small with a large valence-band offset,[7,13] in this case of a commensurately strained sphere the predicted band lineup is clearly type II, with significant offset in both bands. For example, for $x = 0.2$, in the 2D case the conduction-band offset calculated by the same approach is 0.01 eV, less than that caused by the uncertainty in parameters (0.02 eV).

As the direction of stress affects the band alignment for the conduction bands not at Γ, the energy bands of the matrix vary with direction and are plotted in Fig. 4(b) at the spherical boundary $r = R$, from [001] to [111], from [111] to [110], and from [110] to [010] real-space directions. In the [111] direction the conduction bands remain degenerate in their bulk positions and are 0.09 eV higher than the minima in the [100]-like directions, but are still lower than those inside the sphere (which are independent of real-space direction because of the hydrostatic strain inside the sphere). The valence bands change comparatively less with orientation compared to the conduction bands. The valence-band maximum in the matrix is highest in the [111] real-space direction (0.02 eV more than in the [100] direction), so that the conduction-band and valence-band extrema in the matrix lie in different positions in real space. The band gap of the matrix has a minimum at the interface in the [100] direction with a value of 1.03 eV, which is less than that inside the sphere (1.08 eV). The band gap reaches a maximum in the [111] direction in the matrix and is 0.07 eV larger than that in the [100] direction.

Qualitatively similar results are obtained for a long $Si_{0.8}Ge_{0.2}$ cylinder (with its axis in the [001] direction) inside a Si matrix. Figure 5(a) is the band alignment in the [100] real-space direction. Inside the cylinder the energy bands are spatially uniform, but split due to the nonhydrostatic strain. The two conduction-band minima in the [100] k-space directions are 0.06 eV lower in energy than the four in the [010] and [001] k-space directions. The band alignment is type II, with a 0.08-eV conduction-band offset and a 0.14-eV valence-band offset. The energies of the bands in the matrix vary in the different directions in the polar plane in real space, which is given in Fig. 5(b). The six conduction-band minima split into three nondegenerate pairs; bands are only degenerate in the [110] direction. The [100] and [010] directions in real space have the lowest conduction bands ([100] and [010] directions in k space, respectively), which are 0.06 eV lower than that of the [110] direction at the interface $r = R$. The conduction-band edges in the matrix in all real-space directions are lower than that inside the cylinder. Changes for the valence bands in different directions in the matrix are small. The valence-band offset between the [100] and [110] directions in the matrix is 0.02 eV.

A similar analysis was performed for a $Si_{0.8}Ge_{0.2}$ cylinder with its axis in the [011] direction [Fig. 6(a)]. ([011] and [0$\bar{1}$1] are the directions of straight lines usually defined by lithography on (100)-oriented wafers.) Again the bands are spatially uniform inside the cylinder, but four conduction-band minima in k space in the plane of the cylinder lie lower than the other two minima (in the [100] direction) rather than higher. In the matrix the relative alignment of the six conduction-band minimum is also different, as shown in Fig. 6(a). The overall alignment between the inclusion (cylinder) and matrix is again type II, with a 0.11-eV conduction-band
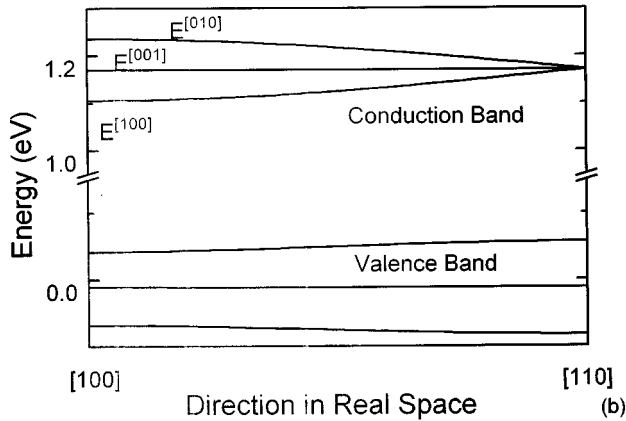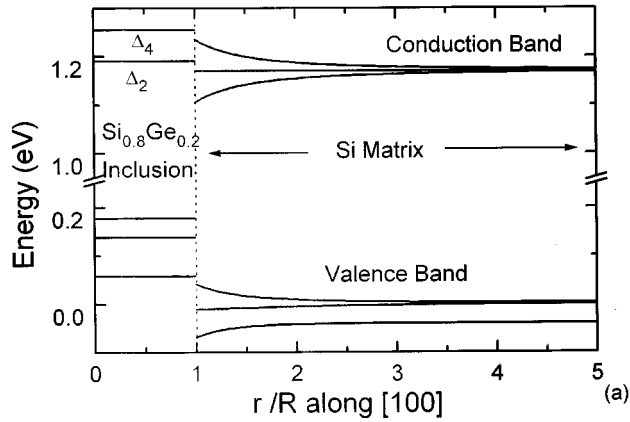
FIG. 5. (a) Band alignments vs r/R in the $[100]$ direction for the 1D system: a $Si_{0.8}Ge_{0.2}$ cylinder inside a Si matrix. The direction of the z axis is in the $[001]$ crystal direction. All energies are plotted as in Fig. 4. (b) Energy bands vs the real-space direction in the matrix at $r=R$.

FIG. 6. (a) Band alignments in the $[1\bar{1}1]$ real space direction for a $Si_{0.8}Ge_{0.2}$ cylinder with the z axis in the $[011]$ direction. All energies are plotted as in Fig. 4. (b) Energy bands vs the real-space direction in the matrix at $r=R$.

offset and a 0.14-eV valence-band offset along $[1\bar{1}1]$. The largest energy offset between the cylinder and matrix for different directions are 0.06 eV for the conduction band and 0.01 eV for the valence band, as plotted in Fig. 6(b).

To summarize these results of band extrema and offsets, Fig. 7 shows the conduction-band and valence-band positions in the $Si_{1-x}Ge_x$ inclusion and in the Si matrix (at $r=R$ in the $[100]$ real-space direction) as a function of Ge concentration in the sphere and cylinder (the z axis in the $[001]$ direction) structures. Also shown for comparison are the band edges of a conventional 2D biaxially strained $Si_{1-x}Ge_x$ layer on a Si(100) substrate (as in Ref. 8) calculated with the parameters in Table I (The $[100]$ real-space direction represents the conduction-band minimum in the Si matrix at $r=R$. Because of the uniform strain in the SiGe in all the three structures, there is no dependence of the conduction-band minimum on the real-space direction in the SiGe in all three cases.) For both 1D and 0D cases, the Δ conduction-band minimum decreases in the matrix and increases in the inclusion, while the valence-band edge increases in the inclusion faster than in the matrix as the Ge concentration increases, in both cases leading to a type-II band alignment. The valence-band maximum in the matrix lies marginally higher in other directions in the 0D and 1D particles as discussed earlier, but not enough to affect the sign of the band offset. For a pure Ge pseudomorphic par-
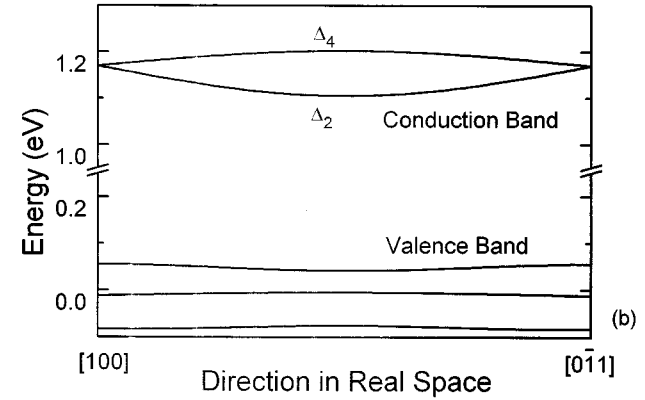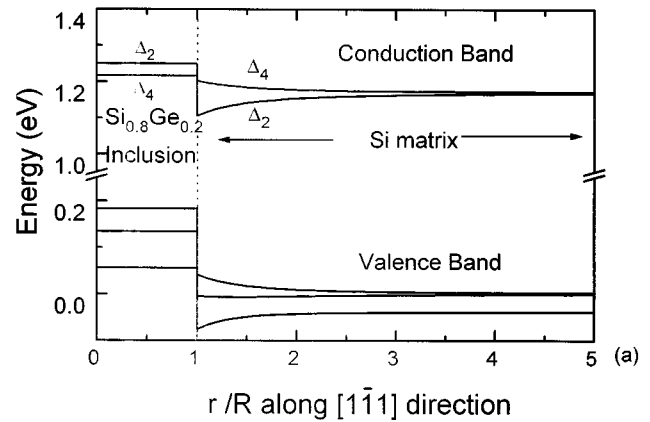
ticle inside a Si matrix, the conduction-band offsets are 0.80 and 0.51 eV and the valence-band offsets are 0.41 and 0.60 eV in the $[100]$ real-space direction for the 0D and 1D cases, respectively. In the conventional 2D case the valence band is higher in the SiGe, as in the 0D and 1D cases. The lack of
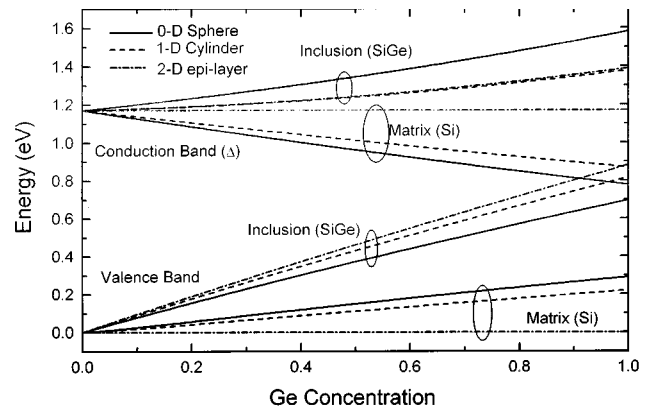

FIG. 7. Valence- and conduction-band edges in a $Si_{1-x}Ge_x$ inclusion and in the Si matrix as a function of the Ge concentration for the 1D cylinder (the axis is in the $[001]$ direction) and 0D sphere structures at the $[100]$ real-space boundary between the matrix and inclusion ($r=R$). The conduction and valence band of a conventional 2D $Si_{1-x}Ge_x$ strained layer on a Si(100) substrate are also shown.

dependence of the Si conduction band on the Ge concentration in the 2D case leads to a much smaller conduction-band offset in the 2D case compared to the 0D and 1D cases, however. While the exact band distribution will depend on the exact shape of 0D and 1D inclusions, the model sphere and cylinder systems chosen here clearly show that care must be taken when directly relating photoluminescence energies to the band gap of the inclusions, as the band type in these structures can be strongly type II.

B. Anisotropy and finite-element modeling

In the above calculations we assumed that the elastic properties of the semiconductors are isotropic, i.e., we used only the bulk modulus $K=(C_{11}+2C_{12})/3$ and Poisson's ratio $\nu=C_{12}/(C_{11}+C_{12})$ so that the strain was only a function of r/R. But actual cubic crystal materials are anisotropic, i.e., $c_{11}-c_{12}-2c_{44}\neq0$. We then used finite-element analysis to calculate the strain in the anisotropic case using a commercially available program.[14] The results indicate that there is only a small change of the strain and energy levels from the isotropic results. The energy bands of 1D and 0D $Si_{0.8}Ge_{0.2}$/Si structures shift less than 0.01 eV, which indicates that the isotropic elasticity assumption is good to first order. The results of the strain distribution cannot be simply added to the plots in Figs. 1 and 2 because in the anisotropic structures strain cannot be reduced to two normal components: tangential (ε_{τ}) and radial (ε_r).

V. $Si_{1-x}Ge_x$/Si V-GROOVE STRUCTURES

Recently, the growth and photoluminescence measurements of $Si_{1-x}Ge_x$ quantum wires on a Si substrate with etched V grooves have been reported.[15,16] Strain distributions of a single wire[17] and an array[18] of wires were calculated assuming that the materials are isotropic. Reference 18 also analytically calculated the effect of strain on the overall band gap in wires, but the effect on the individual band edges and electron and hole confinement energies were not reported. In this work we numerically model the strain in quantum-wire structures, fully considering anisotropic material properties, and present effects individually on both conduction and valence bands. We then calculate quantum confinement energies of carriers in their wires as the wire dimensions become small and relate the results to photoluminescence experiments.

We model the V-groove structure as a long wire with a triangular cross section buried in an infinite matrix as shown in Fig. 8. After the Si is etched, a sharp corner between two {111} planes is formed. $Si_{1-x}Ge_x$ is selectively grown on the bottom of the V groove and capped by a Si epitaxial layer. The growth direction is [100] and the axis of the quantum wire is in the [011] direction forming an approximately triangular cross section with its width $\sqrt{2}$ larger than its depth. We assume that the interface is free from any defects and dislocations. The alloy segregation effect, which might cause the alloy to be nonuniform throughout the triangle, is also neglected. Using finite-element analysis,[14] we calculated the strain distribution, which relies only on the shape of the cross section. Once the strain distribution is known, the band alignments are derived from the same methods discussed before. The conduction-band minimum is the twofold Δ_2 band
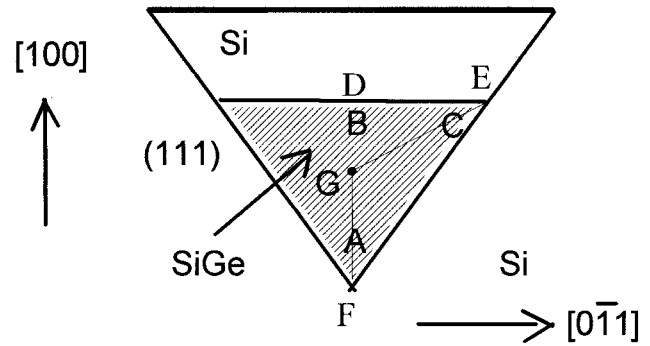

FIG. 8. Cross section of a SiGe epitaxial layer with a Si cap on a V-groove Si(100) substrate.

(in the [100] k-space direction) lying in $Si_{1-x}Ge_x$ near the bottom of the V groove (point A) and the valence-band maximum is the heavy-hole band in the $Si_{1-x}Ge_x$ at the corner of the top interface (point C). Band lineups of the points along the SiGe/Si interface and along the wire cross-section bisector are shown in Fig. 9. The reference energy point is the valence-band edge in Si far from the $Si_{1-x}Ge_x$ interface. Far from SiGe, the conduction-band edge in Si is 1.17 eV. At point A in SiGe, the Δ_2 conduction band is 0.07 eV lower than the lowest conduction-band point in Si, which occurs in the Δ_2 band at point F. At point C, the valence-band edge in

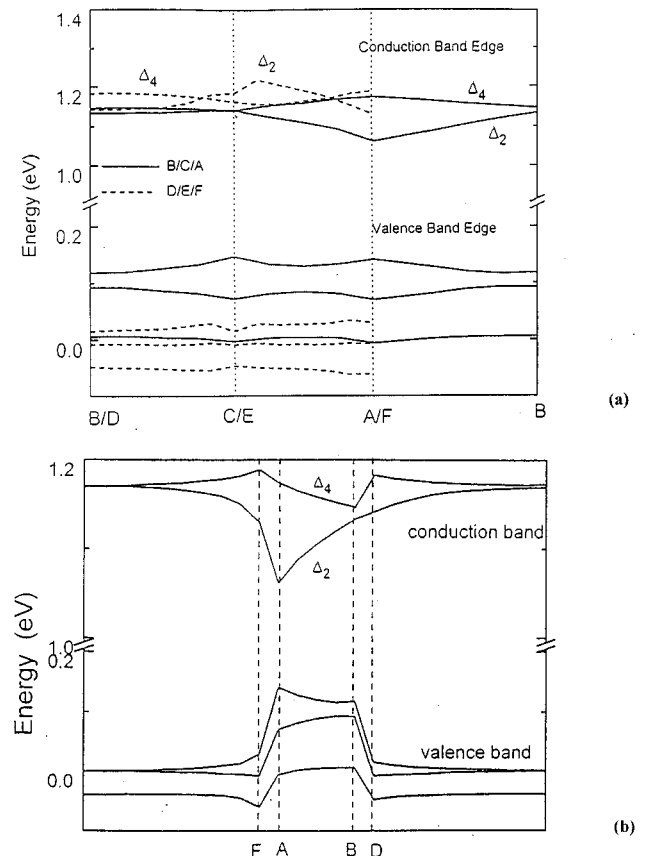FIG. 9. Δ conduction bands and valence bands along (a) the $Si/Si_{0.8}Ge_{0.2}$ interface of the V-groove structure and (b) the vertical wire cross-section bisector. In (a) the solid lines are for points inside SiGe and the dashed lines are for points inside Si.
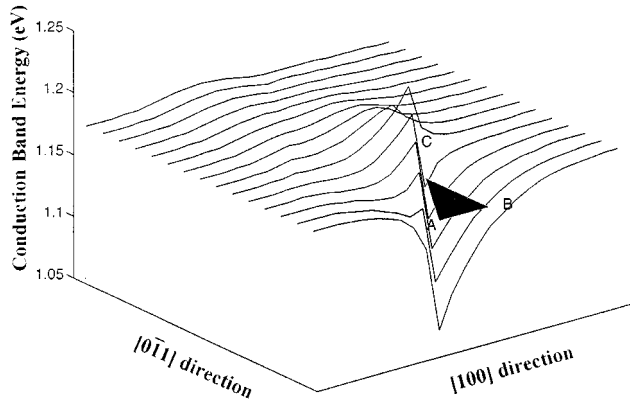
FIG. 10. Δ_2 conduction-band edge of the structure drawn in Fig. 8. The filled triangle shows the area of the $Si_{0.8}Ge_{0.2}$ region. Note that the x and y axes are drawn on different scales.

the $Si_{1-x}Ge_x$ is 0.13 eV higher than point E in Si. A three-dimensional map of the Δ_2 conduction band and the valence-band edge for $Si_{0.8}Ge_{0.2}$ in Si are plotted in Figs. 10 and 11, respectively. In SiGe the Δ_2 bands are lower and the valence-band edges are higher than Si. Note that, as in the case of a symmetric cylinder, holes are confined to SiGe. However, while in the symmetric cylinder case the conduction-band minimum is in the Si matrix, for the V-groove structure the lower conduction band is in SiGe (at point A). This results from the shape of the structure, which causes a large nonhydrostatic strain at point A that splits conduction bands more strongly in the SiGe than in any of the other cases discussed in this paper. The result is the only one in which electrons are strongly confined to SiGe. The conduction bands at point C are not significantly split in the SiGe compared to those at point A because the bisector of the triangle vector at point C (G-C) has a different crystal-line orientation than that for the vector at point A (G-A) and because of the sixfold symmetry of the conduction-band minima.

To consider the quantum confinement effects of a small wire cross section on the electron and hole ground-state energies, the electron and hole confinement energies are estimated using the perturbation approach discussed in Ref. 6 from the 2D potential profiles we calculated from the strain
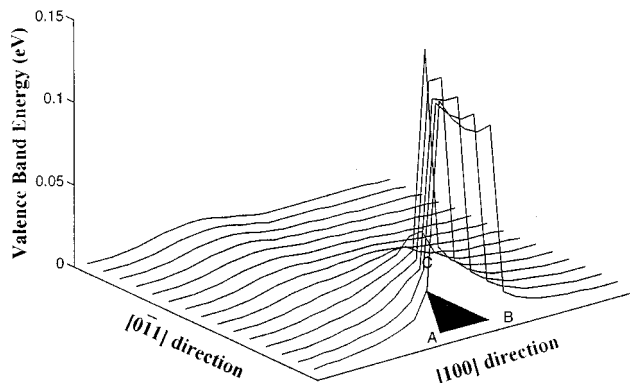

FIG. 11. Valence-band edge of the structure drawn in Fig. 8. The triangle shows the $Si_{0.8}Ge_{0.2}$ region. Note that the x and y axes are drawn on different scales.
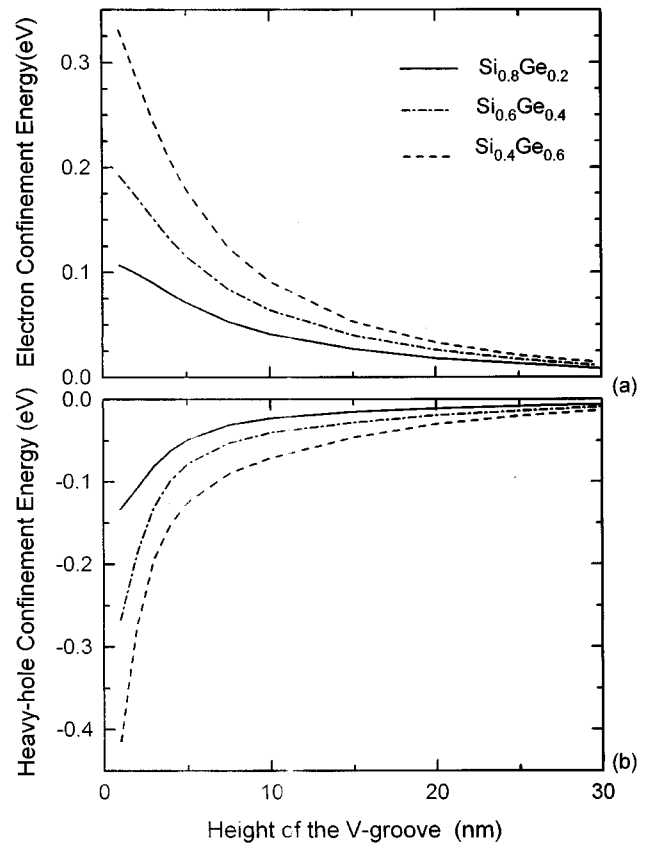

FIG. 12. Confinement energies (energy difference from the ground state of a large structure) of (a) electrons and (b) heavy holes as a function of the height of the SiGe V-groove structure with Ge concentrations of 20%, 40%, and 60%.

fields. Here the electric-field effect and strain effect on the coupling between upper valence bands are neglected. First the 1D Schrödinger equation was solved in the [100] direction using a Si longitudinal electron effective mass of 0.98 (for the Δ_2 conduction band in the [100] k direction) and a heavy-hole effective mass of 0.49 at a given position in the [0$\bar{1}$1] direction. The resulting potential profiles as a function of positions in the [0$\bar{1}$1] direction were then solved using a 1D Schrödinger equation (using a transverse Si effective mass of 0.19 and a heavy-hole effective mass of 0.49) to get the approximate energies of the ground states. The effect of Ge on the masses was second order and not considered. The electron and hole confinement energies (energy difference from the ground state of large size) for $Si_{0.8}Ge_{0.2}$, $Si_{0.6}Ge_{0.4}$, and $Si_{0.4}Ge_{0.6}$ quantum wires are shown in Fig. 12. The quantum effect is significant when the height of the SiGe is less than 10 nm. For a 5-nm-high $Si_{0.8}Ge_{0.2}$ triangle, the confinement energies of the electron and heavy hole are about 0.07 and 0.05 eV, respectively. The confinement energies (size effect) of the electron and hole increase as Ge concentration increases. For 5-nm-high $Si_{0.6}Ge_{0.4}$ and $Si_{0.4}Ge_{0.6}$ triangles, the electron (heavy-hole) confinement energies increase to 0.12 eV (0.08 eV) and 0.18 eV (0.12 eV), respectively. These calculations can be used to predict the photoluminescence energies of the V grooves. The differences between the energies of the lowest electron and highest hole (heavy hole in this case) states are given in Fig. 13 to first order for different $Si_{1-x}Ge_x$ sizes and x values
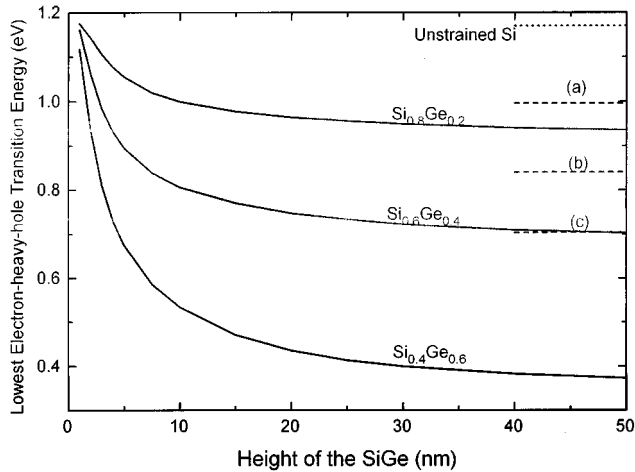
FIG. 13. Lowest transition energies from the electron to the heavy hole as a function of the height of the V-groove $Si_{1-x}Ge_x$ quantum wire with $x=20\%$, 40%, and 60%. The dashed lines show the photoluminescence energies from the 2D conventional $Si_{1-x}Ge_x$ biaxially strained layer with (a) $x=20\%$, (b) $x=40\%$, and (c) $x=60\%$.

(0.2, 0.4, and 0.6). Although the electron and hole wave function will have their maxima in different locations within the SiGe, we neglect any possible resulting electrical-field effects on the transition energy. Any exciton effects are also neglected. First notice that for large SiGe regions, when only strain and not quantum effects are relevant, the transition energies are smaller than those predicted for planar pseudomorphic SiGe layers on Si(100) with the same x (shown for reference as dashed lines). For example, the transition energy is 0.94 eV for a $Si_{0.8}Ge_{0.2}$/Si V-groove structure with a height of 50 nm, compared with the 1.09-eV $Si_{0.8}Ge_{0.2}$ bulk value and the 0.99-eV 2D strained $Si_{0.8}Ge_{0.2}$ epitaxial layer. This larger decrease in transition energy in V-groove structures is mostly due to a significantly lower conduction band and higher valence band in SiGe in the V groove, an effect that does not occur in 2D structures. When the size decreases, the transition energy increases. For $x=20\%$, the transition energy of a triangle less than 7 nm high is predicted to be larger than that of a 2D conventional structure.

VI. SUMMARY

In summary, we have calculated the band lineups of 1D and 0D structures: a sphere, a long cylinder, and V-groove SiGe inside an infinite Si matrix. For $Si_{1-x}Ge_x$ inside a Si matrix, the band alignments are strongly type II for both the sphere and cylinder cases. The conduction-band minima lie in Si matrix and the valence-band maxima lie inside the $Si_{1-x}Ge_x$ inclusion. For the V-groove $Si_{1-x}Ge_x$ one-dimensional structure, the conduction-band minimum and the valence-band maximum are both in SiGe, but at different points in real space. The transition energies from the lowest electron state to the highest heavy-hole state are estimated considering quantum effects. This work demonstrates the importance of accurately accounting for the effects of 3D strain distributions in strained-layer nanostructures and that the relationship of photoluminescence energies to particle compositions may not be straightforward in some cases.

ACKNOWLEDGMENTS

[1] P. Schittenhelm, M. Gail, J. Brunner, J. F. Nützel, and G. Abstreiter, Appl. Phys. Lett. **67**, 1292 (1995).

[2] H. Sunamura, S. Fukatsu, and Y. Shiraki, J. Cryst. Growth **150**, 1038 (1995).

[3] D. Leonard, M. Krishnamurthy, C. M. Reaves, S. P. Denbaars, and P. M. Petroff, Appl. Phys. Lett. **63**, 3203 (1993).

[4] J.-Y. Marzin, J.-M. Gérard, A. Izraël, D. Barrier, and G. Bastard, Phys. Rev. Lett. **73**, 716 (1994).

[5] M. Grundmann, O. Stier, and D. Bimberg, Phys. Rev. B **52**, 11 969 (1995); **50**, 14 187 (1994).

[6] E. Kapon, D. M. Hwang, and R. Bhat, Phys. Rev. Lett. **63**, 430 (1989).

[7] Chris G. Van de Walle and Richard M. Martin, Phys. Rev. B **34**, 5621 (1986).

[8] Chris G. Van de Walle, Phys. Rev. B **39**, 1871 (1989).

[9] Fred H. Pollak and Manuel Cardona, Phys. Rev. **172**, 816 (1968).

[10] J. D. Eshelby, J. Appl. Phys. **25**, 255 (1954).

[11] J. D. Eshelby, Solid State Phys. **3**, 79 (1956).

[12] S. Timoshenko and J. N. Goodier, *Theory of Elasticity* (McGraw-Hill, New York, 1970).

[13] D. C. Houghton, G. C. Aers, S.-R. Eric Yang, E. Wang, and N. L. Rowell, Phys. Rev. Lett. **75**, 866 (1995).

[14] Jean H. Prevost, DYNAFLOW: a nonlinear transient finite-element analysis program. Department of Civil Engineering and Operations Research, Princeton University, 1981; last update 1996.

[15] A. Hartmann, L. Vescan, C. Dieker, and H. Luth, J. Appl. Phys. **77**, 1959 (1995).

[16] N. Usami, T. Mine, S. Fukatsu, and Y. Shiraki, Appl. Phys. Lett. **64**, 1126 (1994).

[17] T. J. Gosling, and J. R. Willis, J. Appl. Phys. **77**, 5601 (1995).

[18] D. A. Faux, J. R. Downes, and E. P. O'Reilly, J. Appl. Phys. **80**, 2515 (1996).

[19] J. Weber and M. I. Alonso, Phys. Rev. B **40**, 5683 (1989).